Journal of Iron and Steel Research, International 24 (2017) 34−42

Contents lists available at ScienceDirect

Journal of Iron and Steel Research, International

journal homepage: www.chinamet.cn

Reduction behavior and mechanism of Hongge vanadium titanomagnetite pellets by gas mixture of H_2 and CO

Wei Li, Gui-qin Fu, Man-sheng Chu, Miao-yong Zhu*
School of Metallurgy, Northeastern University, Shenyang 110819, Liaoning, China

ARTICLE INFO

Key words:
Hongge vanadium titanomagnetite
Pellet
Gas-based direct reduction
Behavior and mechanism
Kinetics

ABSTRACT

Hongge vanadium titanomagnetite (HVTM) pellets were reduced by H_2-CO gas mixture for simulating the reduction processes of Midrex and HYL-III shaft furnaces. The influences of reduction temperature, ratio of $\varphi(H_2)$ to $\varphi(CO)$, and pellet size on the reduction of HVTM pellets were evaluated in detail and the reduction reaction kinetics was investigated. The results show that both the reduction degree and reduction rate can be improved with increasing the reduction temperature and the H_2 content as well as decreasing the pellet size. The rational reduction parameters are reduction temperature of 1050 ℃, ratio of $\varphi(H_2)$ to $\varphi(CO)$ of 2.5, and pellet diameter in the range of 8−11 mm. Under these conditions (pellet diameter of 11 mm), final reduction degree of 95.51% is achieved. The X-ray diffraction (XRD) pattern shows that the main phases of final reduced pellets under these conditions (pellet diameter of 11 mm) are reduced iron and rutile. The peak intensity of reduced iron increases obviously with the increase in the reduction temperature. Besides, relatively high reduction temperature promotes the migration and coarsening of metallic iron particles and improves the distribution of vanadium and chromium in the reduced iron, which is conducive to subsequent melting separation. At the early stage, the reduction process is controlled by interfacial chemical reaction and the apparent activation energy is 60.78 kJ/mol. The reduction process is controlled by both interfacial chemical reaction and internal diffusion at the final stage, and the apparent activation energy is 30.54 kJ/mol.

1. Introduction

The Hongge mining area in Panxi region of southwest China is endowed with 3.55 billion tons of vanadium titanomagnetite resources with high content of chrome[1,2], and it is also recognized as the largest chromium-bearing deposit, which amounts to 9 million tons, accounting for 68% of the chromium reserve in China[3]. Since the chemical composition and phase structure of Hongge vanadium titanomagnetite (HVTM) are much more complicated than those of other vanadium titanomagnetites, it is more difficult to achieve high-efficiency utilization[3], and therefore, HVTM has not been put into practical industrial production. With the continuous consumption of high-grade iron ore resources, large-scale development and utilization of HVTM is becoming highly significant[4].

At present, most vanadium titanomagnetite is smelted in blast furnaces at Panzhihua Iron and Steel Corporation, China[5]. In the blast furnace process, concentrates are sintered or pelletized and smelted to produce hot metal and slag, and the slag is more difficult to be utilized efficiently in traditional separation processes[6,7]. The hot metal obtained from blast furnaces is oxidized to produce vanadium slag, where chromium also exists in the form of spinel. It is more difficult to obtain vanadium and chromium efficiently by sodium salt roasting-water leaching process because of stable spinel structure, which also causes serious environment degradation in soil and water[8-10].

In order to utilize the HVTM efficiently, a new process is proposed for comprehensive utilization of HVTM. In this process, HVTM was firstly pelletized, reduced in shaft furnace, and then melting separated to produce metal phase and molten slag. The metal phase was used as raw materials for steel making or

* Corresponding author. Prof., Ph.D.
E-mail address: *myzhu@mail.neu.edu.cn* (*M.Y. Zhu*).

Received 3 April 2016; Received in revised form 28 June 2016; Accepted 30 June 2016
Available online 15 January 2017

casting and slag needed further treatment for recovering titanium, vanadium, and chromium. The focus of the present study is on the simulation of the direction reduction process of the HVTM pellets in shaft furnace. The factors that affect the reduction degree and rate, phase composition and morphology change were investigated. Furthermore, the reaction kinetics was discussed. The results can provide a theoretical basis and technical support for the comprehensive utilization of HVTM, and increase the recovery rates of vanadium, titanium, and chromium.

2. Experimental

2.1. Experimental materials

In this experiment, the green pellets were prepared and dried for 5 h at 105 ℃ in a drying cabinet. The dried pellets were preheated at 900 ℃, roasted at 1200 ℃ for 15 min in a muffle furnace with an air stream blown in, and then cooled to ambient temperature. The chemical composition of pellets, whose compressive strength was about 2893 N on average, is shown in Table 1.

The mineralogical components of the product pellets were investigated by X-ray diffraction (XRD) analysis (Fig. 1). As shown in Fig. 1, the dominant iron phase is Fe_2O_3 and the majorities of titanium and chromium mainly exist in the form of solid solution Fe_9TiO_{15}, $(Fe_{0.6}Cr_{0.4})_2O_4$, and $Fe_{0.7}Cr_{1.3}O_3$. Besides, chromium is also combined with vanadium in a solid solution $(Cr_{0.15}V_{0.85})_2O_3$. The scanning electron microscopy (SEM) and energy-dispersive spectrometry (EDS) results are shown in Fig. 2. The gases (H_2, CO, CO_2, and N_2) used in the investigation are of 99.99% purity.

Table 1
Chemical composition of HVTM pellets (mass%)

TFe	FeO	CaO	SiO_2	MgO	Al_2O_3	TiO_2	V_2O_5	Cr_2O_3
54.40	0.81	0.73	4.20	2.43	2.38	9.11	0.61	1.48

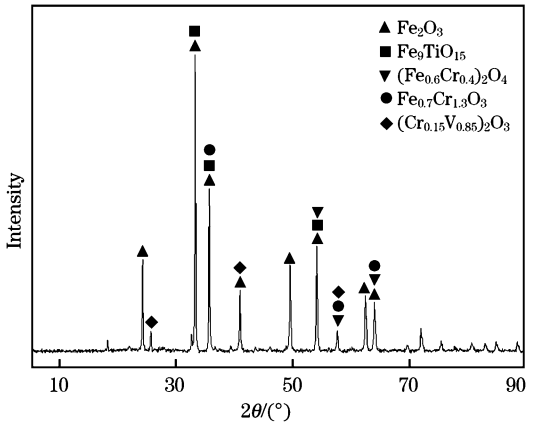

Fig. 1. XRD pattern of HVTM pellets.

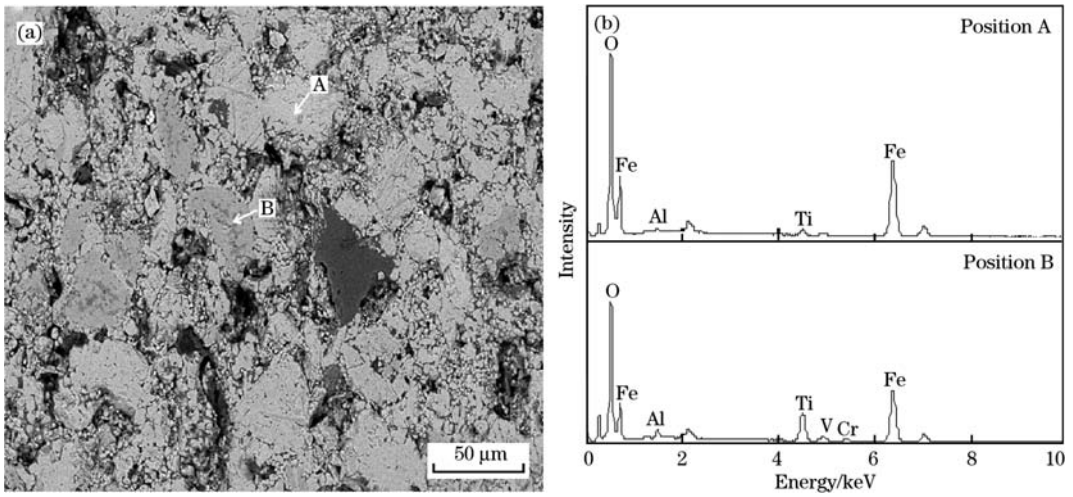

Fig. 2. SEM image (a) and EDS analysis (b) of HVTM pellets.

2.2. Apparatus and procedure

Reduction experiments were conducted in a high-temperature electric resistance furnace to simulate the shaft furnace production process. The schematic diagram of experimental apparatus is shown in Fig. 3. It consists of the main body, a temperature control cabinet, a water drier, and an electronic balance with a detection precision of 1 mg. The gas composition (90%(H_2 + CO) + 5%N_2 + 5%CO_2) was obtained according to the rules of Midrex and HYL-III shaft furnaces and controlled by mass flow controller.

In each experiment, when the shaft furnace was heated to the preset temperature in a pure nitrogen atmosphere, the crucible containing twenty oxidized pellets was put into the furnace and connected to an electronic balance for continuous measurement of the mass loss as a function of time. After stabilization

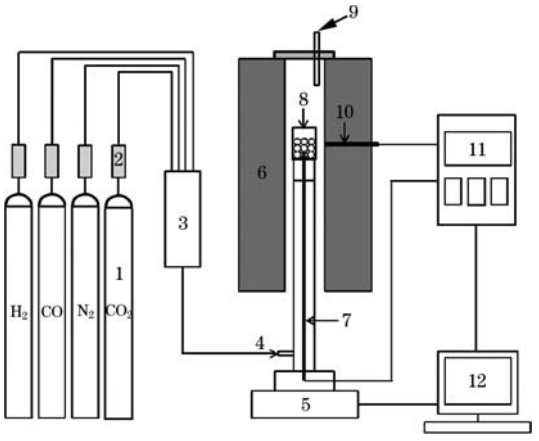

1—Gas containers; 2—Driers; 3—Mass flow controllers; 4—Gas inlet; 5—Electronic balance; 6—Shaft furnace; 7, 10—Thermocouple; 8—Crucible; 9—Gas outlet; 11—Temperature controller; 12—Computer.

Fig. 3. Schematic diagram of experimental apparatus.

of the temperature, reducing gas was introduced into the furnace. When the experiments were finished, the pellets were immediately taken out of the furnace and cooled to room temperature under the protection of argon atmosphere.

After the experiments, the phases of the reduced pellets were analyzed by XRD and the microstructures of the reduced pellets were observed by using a scanning electron microscope equipped with an energy-dispersive spectroscope.

2.3. Definition of reduction degree and reduction rate

In this study, the reduction degree (R) is the mass percentage of oxygen that is reduced from Fe_2O_3 and is calculated by the following formula:

$$R=\left[\frac{0.11w_1}{0.43w_2}+\frac{m_1-m_t}{m_0w_2\times 0.43}\times 100\right]\times 100\% \quad (1)$$

where, w_1 is the ferrous content in the oxidized pellet; w_2 is the content of total iron before reduction; m_0 is the initial mass of pellet; m_1 is the initial mass of pellet after removal of moisture; m_t is the mass of pellet at time t; and 0.11 and 0.43 are conversion coefficients.

The reduction rate (r) can be obtained by differentiating the reduction degree with respect to reduction time in Eq. (2).

$$r=\frac{dR}{dt}=\frac{\Delta R}{\Delta t}=\frac{R_{t+\Delta t}-R_t}{\Delta t} \quad (2)$$

where, ΔR is the difference of reduction degree in each time interval; and Δt is the time interval.

3. Results and Discussion

3.1. Effect of reduction temperature

To show the effect of reduction temperature on reduction degree of HVTM pellets clearly, a series of reduction experiments were carried out at different reduction temperatures from 900 to 1100 ℃ by keeping the ratio of $\varphi(H_2)$ to $\varphi(CO)$ at 2.5 and the pellet diameter at 11 mm. The changes of reduction degree with time at different temperatures are shown in Fig. 4. It can be seen that the reduction degree rises up quickly with increasing the reduction temperature. From the kinetic view, increasing the reduction temperature can improve the rate constant of direct reduction by H_2 and CO. The results show that the final reduction degree increases from 77.43% to 88.46% when the reduction temperature increases from 900 to 1000 ℃. The reduction of pellets has been further enhanced at 1050 ℃, with the final reduction degree of 95.51%. When the reduction temperature exceeds 1050 ℃, further increasing the reduction temperature has slight influence on the reduction degree and the reduction reaction is almost completed. It should be noted that compared with ordinary iron ores, the HVTM pellets are more difficult to be reduced and the final reduction degree could not reach 100% because of the complex chemical composition and special mineral structure.

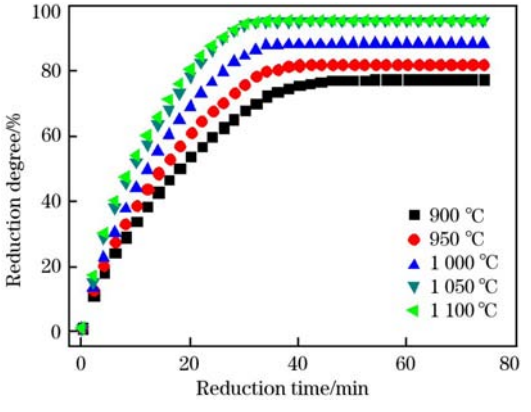

Fig. 4. Reduction degrees of HVTM pellets at various temperatures.

To highlight the influence of reduction temperature on reduction process, the relationship between reduction rate and reduction degree was calculated, as shown in Fig. 5. It is obvious that the reduction temperature apparently promotes the reduction and the reduction rate increases gradually with the increase in reduction temperature. The curves of reduction rate versus reduction degree at different reduction temperatures present an analogous trend. The reduction rate increases sharply when the reduction degree is within 10%, while it decreases considerably in the reduction degree range of 10%－50%, and then turns to steady when the reduction degree is larger than 50%. Considering energy consumption and demand of practical production, a reduction temperature of 1050 ℃ is sufficient for the reduction process.

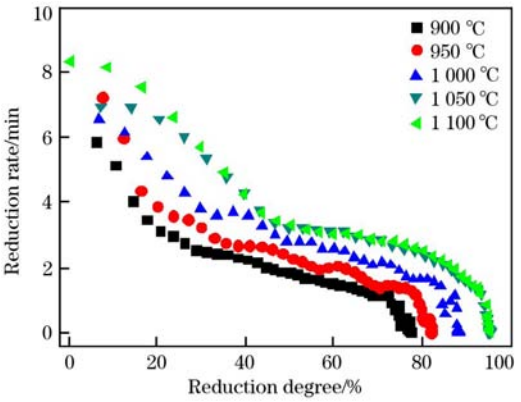

Fig. 5. Reduction rate versus reduction degree at various temperatures.

3.2. Effect of gas composition

Keeping the reduction temperature at 1050 ℃ and the pellet diameter at 11 mm, the variations of reduction degree versus the ratio of $\varphi(H_2)$ to $\varphi(CO)$ between 0.4 and 2.5 are shown in Fig. 6. It indicates that gas atmosphere has a pronounced effect on the reduction of pellets. When the ratio of $\varphi(H_2)$ to $\varphi(CO)$ is 0.4, the final reduction degree is only 76.53% after being reduced for 75 min; when the ratio reaches 1.0, the final reduction degree has reached 87.01%. Further increasing H_2 content consistently accelerates the reduction process for the reason that increasing the H_2 content enlarges the interfacial chemical reaction, thereby increasing the reduction degree. And the increase in the reduction degree at a low ratio is more obvious than that at a high ratio.

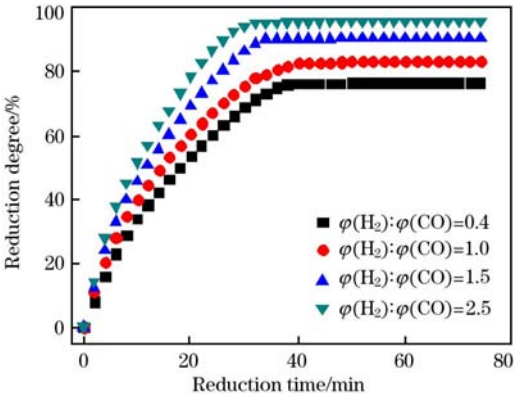

Fig. 6. Reduction degrees of HVTM pellets at various ratios of $\varphi(H_2)$ to $\varphi(CO)$.

Moreover, it can be seen from Fig. 7 that the increase in the ratio of $\varphi(H_2)$ to $\varphi(CO)$ causes a visible increase in the reduction rate. The reduction rate increases with increasing the ratio of $\varphi(H_2)$ to $\varphi(CO)$ in the whole range of the experiment, but it does not increase evidently when the ratio is greater than 1.5. The curves of the reduction rate have almost the same trend with the reduction degree. The reduction rate increases immediately at the initial stage of the experiment when the reduction degree is less than 10%; it then decreases rapidly at the reduction degree in the range of 10%—50%, and finally, it stabilizes at a certain rate as the reduction degree further increases.

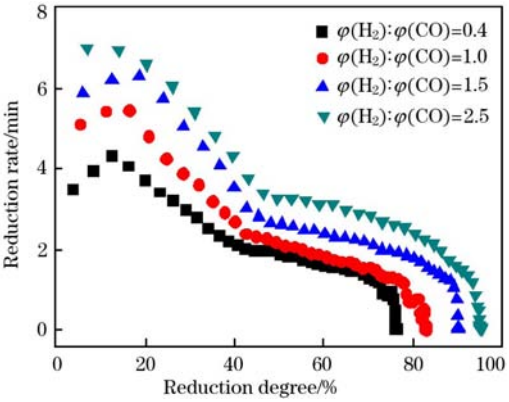

Fig. 7. Reduction rate versus reduction degree at various ratios of $\varphi(H_2)$ to $\varphi(CO)$.

At the initial stage of the reduction process, the reduction rate increases rapidly because of a start effect and the very fast reduction of hematite to magnetite. As the reduction reaction proceeds, a thin layer of ferrous oxides or metallic iron forms. As the reduction reaction further proceeds, a continuous surface layer of metallic iron is produced and becomes thick, impeding gas diffusion, and the reduction rate consequently decreases. Therefore, in order to improve the reduction degree of HVTM pellets, a reasonable ratio of $\varphi(H_2)$ to $\varphi(CO)$ is necessary.

3.3. Effect of pellet size

When the reduction temperature was kept at 1050 ℃ and the ratio of $\varphi(H_2)$ to $\varphi(CO)$ was fixed at 2.5, reduction tests were conducted to investigate the effect of pellet size on the reduction degree. Fig. 8 depicts the variations of reduction degree versus time with different pellet diameters. It is obvious that smaller pellet diameter corresponds to a higher reduction rate; after 30 min, the reduction degree of the pellet of 8 and 11 mm in diameter is more than 90%, while it is less than 80% for the pellet of 17 mm in diameter. The final reduction degree decreases from 95.62% to 87.22% as well with increasing the pellet diameter from 8 to 17 mm. Some investigations[11,12] indicate that with the increase in pellet size, the thermal conductivity performance becomes poor, which greatly leads to the decline in the reduction degree. In addition, the increase in pellet diameter also reduces specific surface area, which has an adverse effect on the diffusion of reducing gas inside the pellets, resulting in the decrease in the reduction

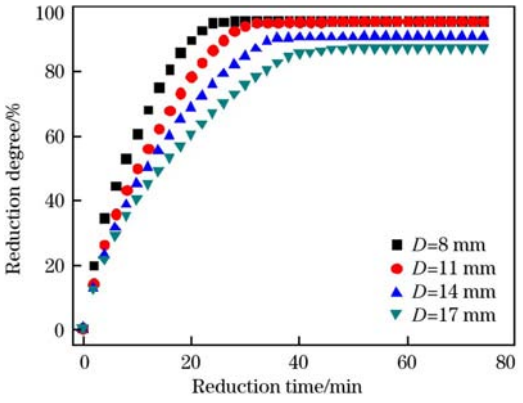

Fig. 8. Reduction degrees of HVTM pellets at various diameters of pellet.

degree. Therefore, to achieve a better reduction degree, the diameter range of 8—11 mm is recommended for practical industrial production of pellets.

3.4. Phases of reduced pellets

To illustrate the effect of reduction temperature on phase transformation, XRD was used to examine the pellets after reaction at 900—1050 ℃ for 60 min when the ratio of $\varphi(H_2)$ to $\varphi(CO)$ was 2.5 and the pellet diameter was 11 mm. The results are shown in Fig. 9. It indicates that with rising the reduction temperatures, the peak intensity of reduced iron increases obviously as iron oxides are reduced gradually. The phases of the pellets reduced at 900 ℃ mainly consist of reduced Fe, Fe_2TiO_4, Fe_2VO_4, and $FeCr_2O_4$.

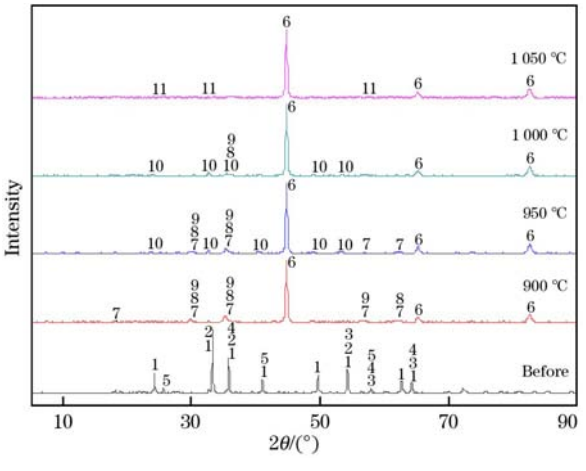

1—Fe_2O_3; 2—Fe_9TiO_{15}; 3—$(Fe_{0.6}Cr_{0.4})_2O_4$; 4—$Fe_{0.7}Cr_{1.3}O_3$; 5—$(Cr_{0.15}V_{0.85})_2O_3$; 6—Fe; 7—Fe_2TiO_4; 8—Fe_2VO_4; 9—$FeCr_2O_4$; 10—$FeTiO_3$; 11—TiO_2.

Fig. 9. XRD patterns of samples reduced at different temperatures for 60 min.

When the reduction temperature is 950 ℃, $FeTiO_3$ peaks appear and Fe_2TiO_4 peaks become weak, which means that the content of $FeTiO_3$ rises and that of Fe_2TiO_4 falls. With increasing the reduction temperature from 950 to 1000 ℃, the peak intensity of $FeTiO_3$ becomes strong, while the Fe_2TiO_4 peaks disappear, which suggests that Fe_2TiO_4 is reduced completely, with the formation of Fe and $FeTiO_3$. At 1050 ℃, titanium oxide phase is observed. It should be mentioned that other valuable elements are not detected by XRD at 1050 ℃. This is probably because the concentrations of vanadium and chromium, as well as some iron oxides, are below a detectable level of XRD technique, which will be discussed later. These results show that high reduction temperature is favorable for the reduction of HVTM pellets. The results are consistent with the aforementioned analysis.

3.5. Morphologies of reduced pellets

After the reaction, four pellets reduced at 900—1050 ℃ for 60 min were randomly selected to be polished with the diamond paste, with the polished surface exposing to the circular section across the center of the sphere, and being sputter-coated with gold and used for SEM and EDS analysis.

Fig. 10 shows the morphologies and EDS results of the pellets reduced at 900 ℃. Basically, there are three morphological regions, i.e., white phase, gray phase, and black phase. The EDS analysis indicates that the white region is mainly composed of iron phase, the dark region is the slag phase, and the gray region comprises mainly of elements Fe, Ti, and O. It is also observed that metallic iron is formed at the presence of macro- and micropores due to the oxygen removal, and integrated tightly with unreduced phases owing to the low reduction temperature. It can also be seen that the distribution relationships between metallic iron and slag phases are very complicated, and slag phases are embraced by metallic iron particles.

Fig. 11 shows the SEM images and EDS results of pellets reduced at 950—1050 ℃. Metallic iron tends to be massive and the growth of the metallic iron particles results in the compact structure of pellet with increasing the reduction temperature. Furthermore, the metallic iron particles are unstable and tend to migrate. High temperature makes newly generated metallic iron particles diffuse and aggregate more freely, which is consistent with the results of the reduction degree and reduction rate. Besides, the boundaries between metallic iron particles and slag phases can be clearly seen. Thus, with the compact metallic iron particles gradually formed and connected to each other, the generation of slag phases and ulvite is hindered, making internal gas diffusion more difficult and hindering the reduction.

This phenomenon can be explained by the minimization of the total surface energy thermodynamically. At high reduction temperatures, accompanying the quick growth, the coalescence of metallic iron crystal

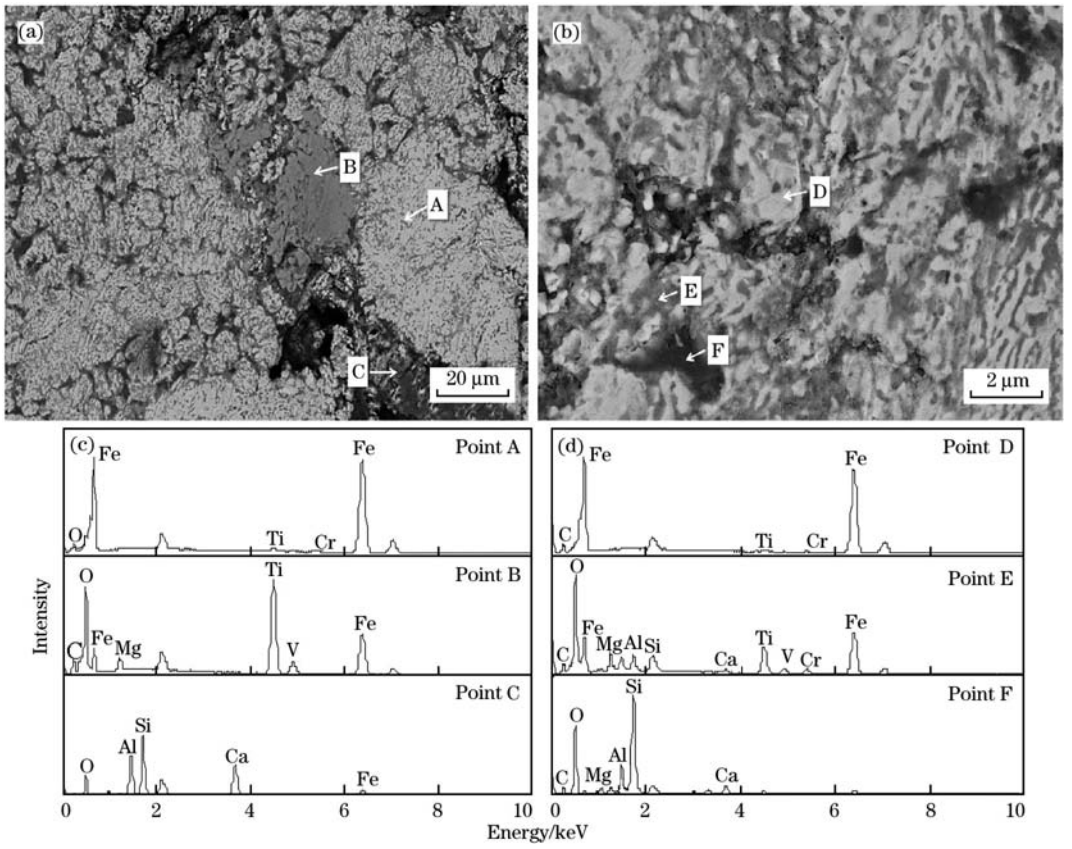

Fig. 10. SEM images (a, b) and EDS analysis (c, d) of pellets reduced at 900 ℃ for 60 min.

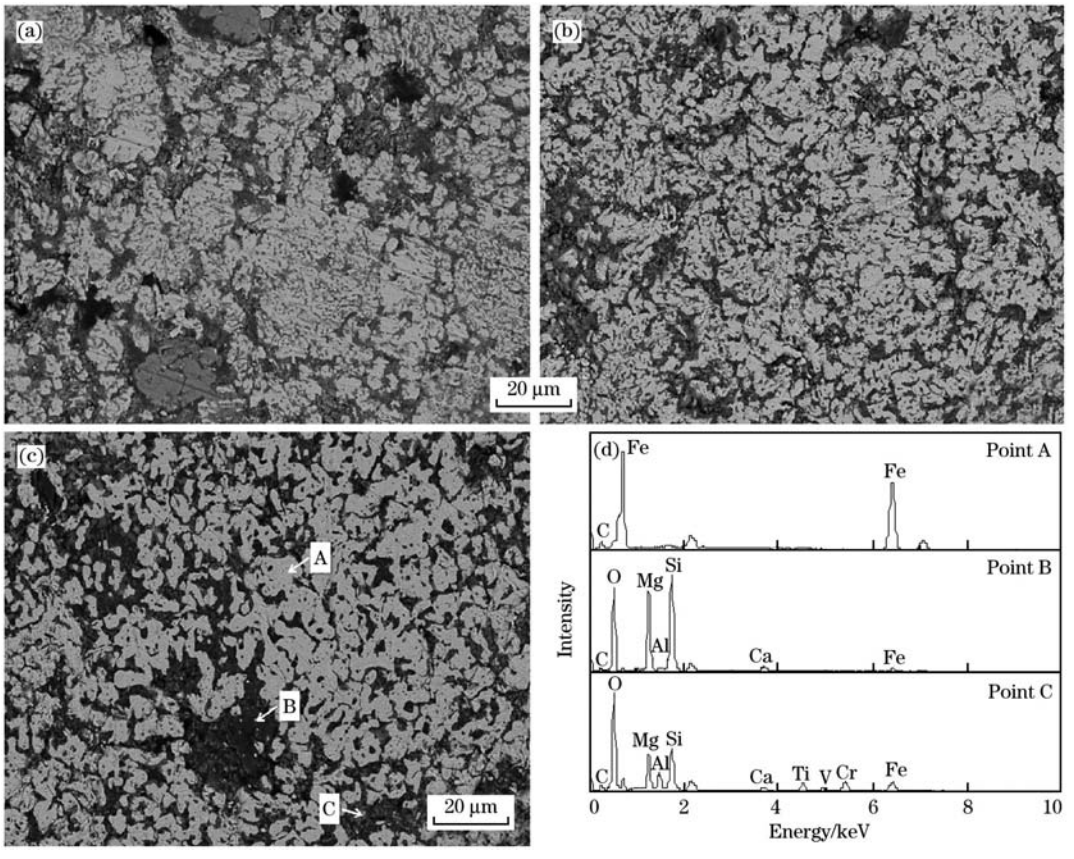

(a) 950 ℃; (b) 1000 ℃; (c) 1050 ℃; (d) EDS analysis of different parts.

Fig. 11. SEM images and EDS analysis of reduced pellets at different temperatures for 60 min.

nucleus and the connections between the metallic iron grains simultaneously happen, the higher rate of reduction is accommodated, and the generated metallic iron is accumulated. When the metallic iron grows up to some extent, the global shape is destroyed. Therefore, iron is mainly in the strip shape and some global iron could also be observed in the reduced pellets. Besides, at 1050 ℃, unreduced iron oxides and ferrum-titanium oxides almost disappear and the coalescence and densification of iron are evident. Different phases are clearly observed in the microstructure, in which considerable quantities of metallic iron shown as white parts (point A) gather, grow up and separate from slag phases (points B and C), and valuable elements like Ti, V, and Cr are also found. However, V and Cr phases are not present in all slag phases.

The elemental mappings were conducted to further clarify the distribution of V and Cr in the reduced product as shown in Fig. 12. It shows that Fe and O are relatively concentrated, and there is an obvious separation between iron and slag phases. Moreover, V and Cr have a similar dispersive distribution in metallic iron. The findings have important implications for the separation of Fe and other valuable elements, particularly for the melting separation method.

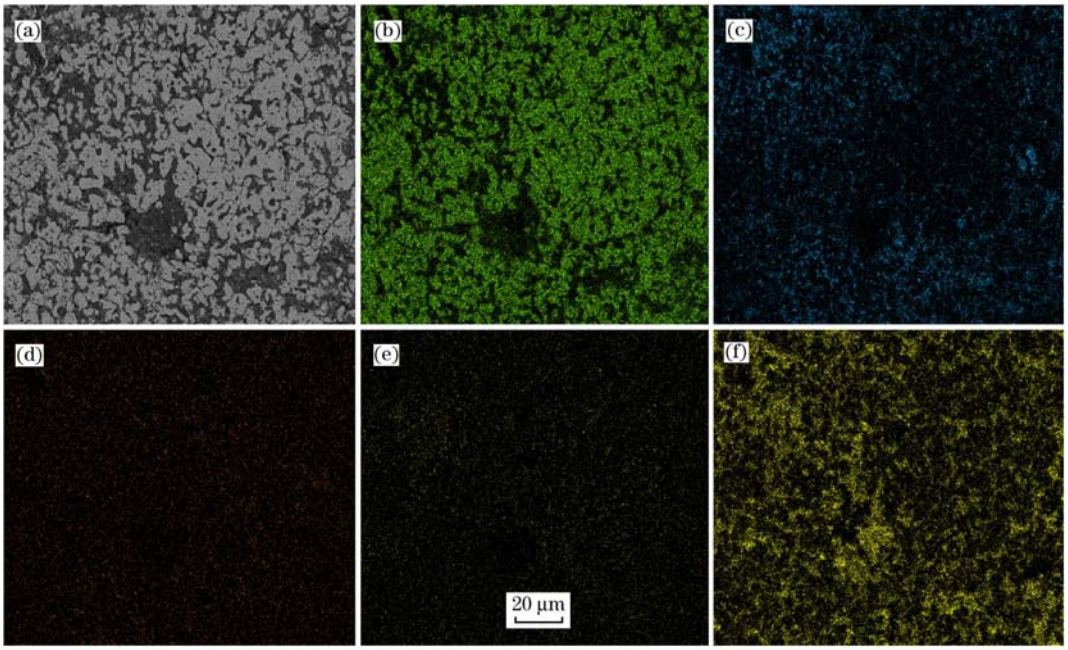

Fig. 12. SEM image of pellets reduced at 1050 ℃ (a) and area mappings of Fe (b), Ti (c), V (d), Cr (e), and O (f).

3.6. Reduction reaction kinetics

According to literatures[13-19], the reduction process of pellets is a typical gas solid reaction that can be described using an approximate unreacted core model. The relationship between R and t is given in Eq. (3)[20,21]:

$$t=\frac{r_0\rho_0 R}{(C_0-C_q)k_g}+\frac{r_0\rho_0}{k(C_0-C_q)}[1-(1-R)^{1/3}]+\frac{r_0^2\rho_0}{D_e(C_0-C_q)}[1/2-R/3-(1-R)^{2/3}/2] \quad (3)$$

where, r_0 is the characteristic initial radius of HVTM pellet, cm; ρ_0 is the density of oxygen of solid phase, mol/cm^3; C_0 is the initial volume concentration of reduction gas, mol/cm^3; C_q is the balance volume concentration of reacting gas, mol/cm^3; k_g is the mass transfer coefficient of gas phase in the phase boundary layer, cm/min; k is the reaction rate constant, cm/min; and D_e is effective diffusion coefficient, cm^2/min.

The first term in the right hand of Eq. (3) refers to the contribution of external diffusion, the second term refers to the contribution of the internal diffusion and the last term shows the contribution of the interfacial chemical reaction. Owing to the critical gas flow adopted, the resistance of external diffusion is negligible and Eq. (3) can be simplified as follows:

$$t=\frac{r_0\rho_0}{k(C_0-C_q)}[1-(1-R)^{1/3}]+\frac{r_0^2\rho_0}{D_e(C_0-C_q)}\cdot[1/2-R/3-(1-R)^{2/3}/2] \quad (4)$$

Given that the reduction of HVTM pellets is a multi-step complex process, C_q is difficult to be determined exactly. $r_0\rho_0/k(C_0-C_q)$ is defined to be equal to $1/k_a$, where k_a is the apparent reaction rate constant. In the following analysis, k appears in the form of first power; thus, there is no effect on relative calculation using k_a.

When the reduction process is controlled by interfacial chemical reaction, based on the results shown in Fig. 4 and applied into Eq. (4), the plots of $[1-(1-R)^{1/3}]$ versus time at different temperatures are shown in Fig. 13. It is found that there is excellent

linear dependence between $[1-(1-R)^{1/3}]$ and t all through the reduction process, indicating that the reaction is controlled by the interfacial chemical reaction. The apparent reaction rate constant is regarded as the slope of the line. The higher the reduction temperature, the higher the apparent reaction rate constant.

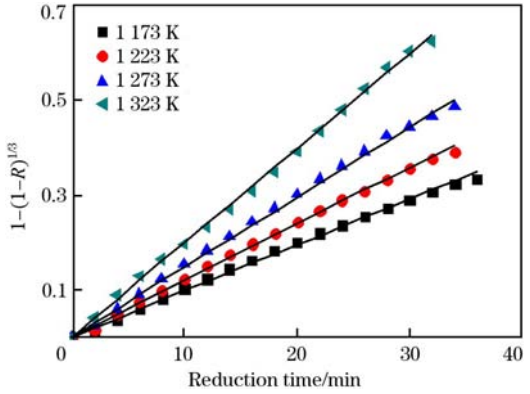

Fig. 13. Relationship between $1-(1-R)^{1/3}$ and t at different temperatures.

If the reduction process is controlled by internal diffusion, the relationship between $[1/2-R/3-(1-R)^{2/3}/2]$ and t could be calculated. The results can be fitted as shown in Fig. 14. It is found that $[1/2-R/3-(1-R)^{2/3}/2]$ is linear with t only at the final stage of reduction, indicating that the reaction is controlled by the internal diffusion. It can also be found that the higher the temperature, the sooner the start time of reaction is controlled by internal diffusion.

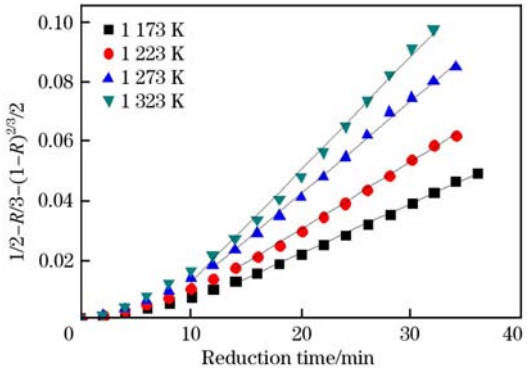

Fig. 14. Relationship between $1/2-R/3-(1-R)^{2/3}/2$ and t at different temperatures.

Supposing that the reduction process is controlled by both interfacial chemical reaction and internal diffusion, and dividing both sides of Eq. (4) by $[1-(1-R)^{1/3}]$, Eq. (4) can be simplified as:

$$\frac{t}{1-(1-R)^{1/3}}=\frac{r_0\rho_0}{k(C_0-C_q)}+\frac{r_0^2\rho_0}{6D_e(C_0-C_q)}\cdot[1+(1-R)^{1/3}-2(1-R)^{2/3}] \quad (5)$$

The relationship between $t/[1-(1-R)^{1/3}]$ and $[1+(1-R)^{1/3}-2(1-R)^{2/3}]$ is shown in Fig. 15. As

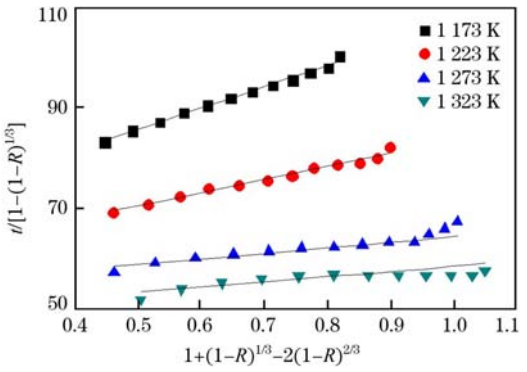

Fig. 15. Relationship between $t/[1-(1-R)^{1/3}]$ and $[1+(1-R)^{1/3}-2(1-R)^{2/3}]$ at different temperatures.

can be seen in Fig. 15, an excellent linear dependence between $t/[1-(1-R)^{1/3}]$ and $[1+(1-R)^{1/3}-2(1-R)^{2/3}]$ is obtained at the final stage, which further proves that the reduction process is controlled by both interfacial chemical reaction and internal diffusion.

According to the Arrhenius equation,

$$k_a=A\exp\left(-\frac{E_a}{RT}\right) \quad (6)$$

where, A is the frequency factor, s^{-1}; E_a is the apparent activation energy, kJ/mol; R is the ideal gas constant, 8.314×10^{-3} kJ/(mol·K); and T is the absolute temperature, K. Taking the logarithm of both sides of Eq. (6), following equation can be obtained:

$$\ln k_a=-\frac{E_a}{RT}+\ln A \quad (7)$$

By plotting $\ln k_a$ against $1/T$, the slope could be used to calculate the apparent activation energy value.

According to the slope in Fig. 13 and Fig. 15, the relationship between $\ln k_a$ and $1/T$ is shown in Fig. 16. Thus, the apparent activation energies are 60.78 kJ/mol at the early stage and 30.54 kJ/mol at the final stage, respectively.

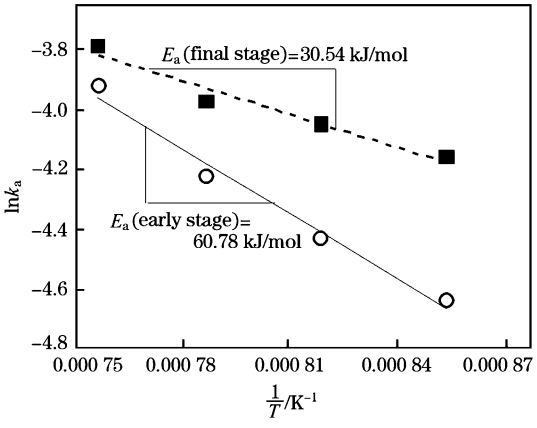

Fig. 16. Arrhenius plot of apparent rate constant for reduction process of pellets.

4. Conclusions

(1) The reduction degree and reduction rate of HVTM pellets increase with the increase in the reduction temperature and the ratio of $\varphi(H_2)$ to $\varphi(CO)$ and the decrease in the pellet diameter.

(2) The rational reduction parameters are reduction temperature of 1050 ℃, ratio of $\varphi(H_2)$ to $\varphi(CO)$ of 2.5, and pellet diameter in the range of 8−11 mm. Under these conditions (pellet diameter of 11 mm), final reduction degree of 95.51% is achieved and the main phases of reduced pellets are reduced iron and rutile.

(3) With the increase in reduction temperature, the peak intensity of metallic iron becomes strong and the metallic iron particles agglomerate; the slag phases are embraced by metallic iron particles and vanadium and chromium dispersively distribute in the reduced iron.

(4) The reduction reaction kinetics by the unreacted core model indicates that the reduction process is controlled by interfacial chemical reaction at the early stage and the apparent activation energy is 60.78 kJ/mol. The reduction process is controlled by both interfacial chemical reaction and internal diffusion at the final stage and the apparent activation energy is 30.54 kJ/mol.

Acknowledgment

This work is financially supported by National Natural Science Foundation of China (Grant No. 51574067).

References

[1] J. H. Luo, Z. Y. Wu, E. H. Wu, J. H. Li, X. J. Liao, R. Tang, S. L. Yang, Iron Steel Vanadium Titanium 36 (2015) No. 2, 73-77 (in Chinese).
[2] H. G. Du, Theory of Smelting Vanadium-bearing Titanomagnetite by Blast Furnace, Science Press, Beijing, 1996 (in Chinese).
[3] J. H. Chen, C. P. Guan, Y. Wang, Y. M. Zhou, X. J. Tang, Sichuan Nonferrous Metallurgy (2011) No. 2, 17-20 (in Chinese).
[4] W. G. Fu, Y. C. Wen, H. E. Xie, J. Iron Steel Res. Int. 18 (2011) No. 4, 7-10, 18.
[5] W. G. Fu, H. E. Xie, Steel Res. Int. 82 (2011) 501-504.
[6] Y. Zhang, J. Tang, M. S. Chu, Y. Liu, S. Y. Chen, X. X. Xue, J. Iron Steel Res. Int. 21 (2014) No. 2, 144-150.
[7] G. H. Han, T. Jiang, Y. B. Zhang, Y. F. Huang, G. H. Li, J. Iron Steel Res. Int. 18 (2011) No. 8, 14-19.
[8] B. Liu, H. Du, S. N. Wang, Y. Zhang, S. L. Zheng, L. J. Li, D. H. Chen, AICHE J. 59 (2013) No. 2, 541-552.
[9] D. S. Chen, L. S. Zhao, T. Qi, G. P. Hu, H. X. Zhao, J. Li, L. N. Wang, Trans. Nonferrous Met. Soc. China 23 (2013) 3076-3082.
[10] Z. H. Wang, S. L. Zheng, S. N. Wang, B. Liu, D. W. Wang, H. Du, Y. Zhang, Trans. Nonferrous Met. Soc. China 24 (2014) 1273-1288.
[11] G. H. Han, T. Jiang, Y. B. Zhang, Y. F. Huang, G. H. Li, J. Iron Steel Res. Int. 18 (2011) No. 8, 14-19.
[12] S. Y. Luo, Y. M. Zhou, C. J. Yi, J. Renew Sustain Ener. 5 (2013) No. 6, 063114.
[13] H. W. Kang, W. S. Chung, T. Murayama, Y. Ono, ISIJ Int. 38 (1998) 324-331.
[14] H. B. Zuo, C. Wang, J. J. Dong, K. X. Jiao, R. S. Xu, Int. J. Miner. Metall. Mater. 22 (2015) 688-696.
[15] J. H. Liu, J. Y. Zhang, T. P. Zhou, J. Iron Steel Res. 12 (2000) No. 1, 5-9 (in Chinese).
[16] A. Bonalde, A. Henriquez, M. Manrique, ISIJ Int. 45 (2005) 1255-1260.
[17] H. T. Wang, H. Y. Sohn, Metall. Mater. Trans. B 44 (2013) 133-145.
[18] A. Habermann, F. Winter, H. Hofbauer, J. Zirngast, J. L. Schenk, ISIJ Int. 40 (2000) 935-942.
[19] H. M. Long, J. X. Li, P. Wang, S. Q. Shi, Ironmak. Steelmak. 39 (2012) 585-592.
[20] E. A. Mousa, A. Babich, D. Senk, Steel Res. Int. 84 (2013) 1085-1097.
[21] H. Y. Sun, J. S. Wang, Y. H. Han, X. F. She, Q. G. Xue, Int. J. Miner. Process. 125 (2013) 122-128.